Quadrotor Takeoff Trajectory Planning in a One-Dimensional Uncertain Wind-field Aided by Wind-Sensing Infrastructure

Nicholas Kakavitsas*, Artur Wolek[†] *University of North Carolina at Charlotte, Charlotte, North Carolina*, 28223

This paper investigates optimal takeoff trajectory planning for a quadrotor modeled with vertical-plane rigid body dynamics in an uncertain, one-dimensional wind-field. The wind-field varies horizontally and propagates across an operating region with a known fixed speed. The operating area of the quadrotor is equipped with wind-sensing infrastructure that shares noisy anemometer measurements with a centralized trajectory planner. The measurements are assimilated via Gaussian process regression to predict the wind at unsampled locations and future time instants. A minimum-time optimal control problem is formulated for the quadrotor to take off and reach a desired vertical-plane position in the presence of the predicted wind-field. The problem is solved using numerical optimal control. Several examples illustrate and compare the performance of the trajectory planner under varying wind conditions and sensing characteristics.

I. Nomenclature

O	=	origin of inertial reference frame			
I	=	inertial reference frame; $\{O, i_1, i_2, i_3\}$			
G	=	center of mass of the quadrotor			
${\mathcal B}$	=	body reference frame; $\{G, \boldsymbol{b}_1, \boldsymbol{b}_2, \boldsymbol{b}_3\}$			
l	=	distance between propellers			
$T_{ m r},T_{ m f}$	=	equivalent thrust for two rear and forward motors, respectively			
$T_{ m max}$	=	maximum thrust limit			
v	=	inertial velocity			
$v_{\rm r}$	=	flow-relative velocity			
v_{δ}	=	wind velocity			
Θ	=	vector of roll, pitch, and yaw Euler angles, respectively; $[\phi, \theta, \psi]^T$			
$R(\mathbf{\Theta})$	=	yaw-pitch-roll rotation matrix			
x	=	inertial position vector of the quadrotor expressed in \mathcal{I}			
ω	=	angular velocity of \mathcal{B} frame with respect to \mathcal{I} frame; $[p,q,r]^{\mathrm{T}}$			
$L(\mathbf{\Theta})$	=	transformation matrix relating $\dot{\mathbf{\Theta}}$ and $\boldsymbol{\omega}$			
$C_{\mathrm{D},(\cdot)}$	=	coefficient of drag in the (\cdot) body frame direction			
$A_{(\cdot)}$	=	wetted surface area in the (\cdot) body frame direction			
m	=	quadrotor mass			
$f_{(\cdot)}$	=	force summation in the respective (\cdot) body frame direction			
$ au_{(\cdot)}$	=	moment summation about the respective (\cdot) body frame axis			
u	=	control input vector; $[T_f, T_r]^T$			
I	=	vehicle mass moment of inertia matrix			
I_{22}	=	pitch-axis mass moment of inertia			
$m{f}_{net}$	=	vector of net body-frame forces; $[f_1, f_2, f_3]^T$			
$ au_{ m net}$	=	vector of net body-frame moments; $[\tau_1, \tau_2, \tau_3]^T$			
$p_{ m N}, p_{ m D}$	=	position north and down, respectively			
$\delta_{ m N}, \delta_{ m D}$	=	wind velocity north and down, respectively			
t_k	=	discretized time at kth time step			

^{*}Graduate Student, Department of Mechanical Engineering and Engineering Science, nkakavit@charlotte.edu, AIAA Student Member.

Assistant Professor, Department of Mechanical Engineering and Engineering Science, awolek@charlotte.edu, AIAA Member.

```
u_{\rm r}, v_{\rm r}, w_{\rm r}
                   flow-relative velocity expressed along \mathcal{B} frame unit vectors b_1, b_2, and b_3, respectively
                   vector of quadrotor states at time t_k; [p_{N,k}, p_{D,k}, \theta_k, u_{r,k}, w_{r,k}, q_k]^T
\boldsymbol{x}_k
P
                   translating origin of the wind frame
                   wind reference frame; \{P, p_1, p_2, p_3\}
P
                  speed of the convecting wind-field
                  horizontal coordinate in \mathcal{P} frame
β
\mu(\beta)
                  mean function of the Gaussian process
\kappa(\beta, \beta')
                  kernel function of the Gaussian process
\mathbb{E}[\cdot]
                  expected value operator
                   vector of Gaussian process hyperparameters; [L, \sigma]^T
\theta
                  length scale of Gaussian process
L
\sigma^2
                  variance of Gaussian process
h
                  spatial lag term for squared exponential kernel
                  upper bound on the total anticipated takeoff duration
t_m
                  horizontal length of the operating region
d
                  horizontal length over which the GP wind-field is estimated
λ
A
                   number of anemometers
                  inertial frame horizontal position of the ith anemometers
Z_{i}
                   zero-mean Gaussian measurement noise with variance \sigma_n^2
\epsilon
                   vector of measurements taken by all anemometers at time t_k
\mathbf{y}_k
                   vector of positions of anemometers for each set of measurements at time t_k
\mathbf{s}_k
F
                   sampling rate of anemometers
                   total sampling time of anemometers prior to takeoff
t_N
                   total number of measurements used in GP regression across all anemometers and time
M
f
                   vector of wind-field observations
                   vector of wind-frame locations corresponding to f
β
                   vector of grid points in the wind frame over which the Gaussian process is estimated
g
G
                  total number of grid points g
Y
                   matrix of wind-sensing time, position, and measurement data collected up to time t_N
\hat{\delta}_{\rm N}(\boldsymbol{g};\boldsymbol{Y})
                   wind estimate over g given data Y
                  covariance matrix of the estimate over g given data Y
P_{\delta_{\rm N}}(\boldsymbol{g};\boldsymbol{Y})
                  matrix of covariance values relating observation and/or grid points
                   measurement truncation parameter
                  horizontal interval indicating the zone of measurement acceptance at time t
\phi(t)
                   mean of the wind-field
\mu_w
```

II. Introduction

Wind disturbances can adversely affect small unmanned aerial vehicles (UAVs) by reducing performance, increasing power consumption, and impacting stability. power consumption, and impacting stability—potentially rendering UAVs unable to perform their tasks or leading to dangerous collisions with people or property [1, 2]. Feedback control strategies for multirotor-type UAVs to reject disturbance are well developed [3-6] and can be aided by measuring the wind (e.g., using hot-wire or sonic anemometers [7–9] and multi-hole pressure probes [10, 11]) or by inferring the wind using on-board sensors such as a GPS, IMU, and altimeter [12–16]. Model-based wind estimation techniques have also been proposed [17–20]. While disturbance rejection offers a reactive mechanism to mitigate wind already affecting the vehicle, trajectory planning can avoid or exploit anticipated disturbances at future vehicle positions and thereby provide a proactive wind mitigation strategy to complement feedback control.

Trajectory planning in wind requires a model or estimate of spatiotemporal wind conditions within the operating environment. Spatial wind distributions can be modeled using computational, analytical, and frequency-spectrum models, or by interpolating point measurements provided by wind-sensing infrastructure (e.g., anemometers mounted on structures or other airborne platforms). Numerical weather and wind prediction models that are routinely used at higher altitudes and around airports have inadequate resolution and accuracy in urban environments to support small UAV flight planning [21, 22]. However, some commercial providers [23, 24] offer instrumentation and modeling capabilities for micro-scale wind-field estimation. Computational fluid dynamics (CFD) simulations provide numerical models of wind-fields, for example, via machine learning from CFD data-sets [25] or generalizing pre-computed CFD data-sets to different building morphologies for predicting urban wind-fields [26]. Indeed, prior work has used CFD-based wind models for flight simulation [27–30] and path planning [31–35]. While CFD provides high fidelity simulations of complex wind flows, it is computationally intensive. Analytical or statistical wind and gust models are more amenable for use in real-time estimation, control, and trajectory planning. For example, polynomial [36] or logarithmic [37] functions of altitude, including those with unsteady components driven by colored-noise [38], have been used to model wind conditions. Other examples of analytical wind and gust model include the one-minus-cosine gust model, the power law used to model wind shear, and various wake vortex [39] and parametric models based on potential flow theory [40]. Spectral wind turbulence models such as the Dryden and Von Karman models [41] are widely used for flight dynamics simulations and describe the turbulence characteristics of an aircraft moving at a fixed speed through a spatially "frozen" wind-field [42, 43]. Other models in this category include the random walk model [39] and stochastic Wiener process [44]. Interpolation-based methods have been adopted to model wind-fields and ocean currents using B-splines [45], Kalman filters with spatial basis functions [46, 47], and Gaussian processes [48–51].

This work considers a single quadrotor modeled with rigid-body dynamics that operates in the vertical plane in the presence of an uncertain one-dimensional wind-field. The wind-field is vertically uniform, but varies horizontally according to a Gaussian process (GP) model with an unknown mean. The wind-field propagates through the environment at a constant known speed, and is sampled by several anemometers positioned up-stream from the initial position of the quadrotor. Local wind measurements are shared to collaboratively estimate the global wind-field using Gaussian process regression (a form of spatial interpolation). The resulting estimate is treated as a known time and state-dependent disturbance in formulating a deterministic optimal trajectory planning problem for the quadrotor to take off and reach a desired waypoint in the vertical plane. This problem formulation emulates a scenario wherein a quadrotor exploits information provided by nearby wind-sensing infrastructure. For example, anemometers might be available to sense wind around an airfield or landing pad, or wind information could be provided by other nearby airborne platforms.

The contributions of this paper are: (1) a GP-based estimation framework for using noisy wind-sensing infrastructure in an environment to collaboratively estimate a one-dimensional wind-field that is convecting at a known speed, and (2) formulating a minimum-time takeoff trajectory planning problem for a quadrotor with vertical plane rigid-body dynamics that incorporates estimated wind knowledge. The trajectory planning problem is solved using the pesudeospectral optimal control solver GPOPS-II [52]. The performance of the estimation and trajectory planning framework is compared through simulations that vary the wind strength and variance, and the measurement frequency and noise.

The remainder of the paper is organized as follows. Section III describes the quadrotor motion model, the wind and wind measurement models, and the optimization problem. Section IV describes a Gaussian process approach for estimating the wind-field and a GPOPS-II based trajectory planning. Section V describes the results of numerical simulations that quantify control performance under varying wind conditions and sensor quality. The paper is concluded, and future work is suggested in Section VI.

III. Problem Formulation

This section introduces the vertical plane dynamics of a quadrotor, presents a model for wind-sensing infrastructure measurement, and formulates the optimization problem.

A. Quadrotor Dynamics

Let $I = \{O, i_1, i_2, i_3\}$ be an inertial reference frame with its origin at point O and with orthonormal unit vectors oriented along the north-east-down directions, respectively, as shown in Fig. 1. Let $\mathcal{B} = \{G, b_1, b_2, b_3\}$ be a body reference frame, with its origin centered at the center of mass (G) of the quadrotor, and with orthonormal unit vectors oriented in the forward-right-down body directions, respectively.

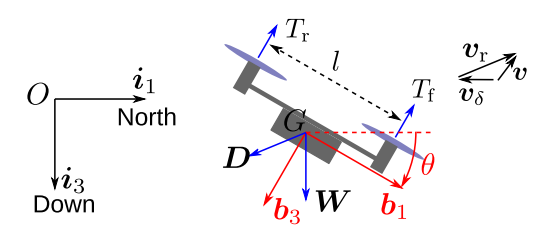


Fig. 1 References frames and quantities used to define the three degree-of-freedom quadrotor model. The wind triangle (upper right) shows the inertial velocity v as the sum of the flow-relative velocity $v_{\rm r}$ and the wind velocity v_{δ} . The quadrotor is drawn with pitch angle $\theta < 0$.

Let $\mathbf{\Theta} = [\psi, \theta, \phi]^{\mathrm{T}}$ be a vector of yaw, pitch, and roll angles respectively. The rotation matrix

$$\boldsymbol{R}(\boldsymbol{\Theta}) = \begin{bmatrix} c_{\theta}c_{\psi} & s_{\phi}s_{\theta}c_{\psi} - c_{\phi}s_{\psi} & c_{\phi}s_{\theta}c_{\psi} + s_{\phi}s_{\psi} \\ c_{\theta}s_{\psi} & s_{\phi}s_{\theta}s_{\psi} + c_{\phi}c_{\psi} & c_{\phi}s_{\theta}s_{\psi} - s_{\phi}c_{\psi} \\ -s_{\theta} & s_{\phi}c_{\theta} & c_{\phi}c_{\theta} \end{bmatrix}$$
(1)

is an element of special orthogonal group, SO(3), and relates the orientation of reference frame \mathcal{B} to I using a 3-2-1 Euler angle sequence, where $c(\cdot) = \cos$, $s(\cdot) = \sin$, are used as shorthand notation. The inertial position of the quadrotor is $\mathbf{x} = [p_{\rm N}, p_{\rm E}, p_{\rm D}]^{\rm T}$ expressed using coordinates in I and the inertial velocity of the quadrotor is $\mathbf{v}^{\mathcal{B}} = [u, v, w]^{\rm T}$ expressed in \mathcal{B} . The inertial velocity is given by the sum

$$v^{\mathcal{B}} = v_{\rm r}^{\mathcal{B}} + v_{\delta}^{\mathcal{B}} \,, \tag{2}$$

where $\mathbf{v}_{r}^{\mathcal{B}} = [u_{r}, v_{r}, w_{r}]^{T}$ is the wind-relative velocity of the quadrotor and $\mathbf{v}_{\delta}^{\mathcal{B}} = [\delta_{1}, \delta_{2}, \delta_{3}]^{T}$ is the wind velocity, both expressed in \mathcal{B} . The inertial velocity in frame I is then $\dot{\mathbf{x}} = \mathbf{v}^{I} = \mathbf{R}(\mathbf{\Theta})\mathbf{v}^{\mathcal{B}}$. Similarly, the wind-velocity in the inertial frame is $\mathbf{v}_{\delta}^{I} = [\delta_{N}, \delta_{E}, \delta_{D}]^{T}$ and is related to the body-frame wind-velocity by

$$\mathbf{v}_{\delta}^{I} = \mathbf{R}(\mathbf{\Theta})\mathbf{v}_{\delta}^{\mathcal{B}} . \tag{3}$$

The vector $\boldsymbol{\omega} = [p,q,r]^{\mathrm{T}}$ is the angular velocity of the quadrotor body-frame with respect to the inertial frame, where p, q, and r are the roll, pitch, and yaw rates, respectively. The Euler rates $\dot{\boldsymbol{\Theta}} = \left[\dot{\phi},\dot{\theta},\dot{\psi}\right]^{\mathrm{T}}$ are related to $\boldsymbol{\omega}$ by $\dot{\boldsymbol{\Theta}} = \boldsymbol{L}(\boldsymbol{\Theta})\boldsymbol{\omega}$ where

$$\boldsymbol{L}(\boldsymbol{\Theta}) = \begin{bmatrix} 1 & s_{\phi}t_{\theta} & c_{\phi}t_{\theta} \\ 0 & c_{\phi} & -s_{\phi} \\ 0 & s_{\phi}/c_{\theta} & c_{\phi}/c_{\theta} \end{bmatrix} . \tag{4}$$

The Newton-Euler equations of motion for the system are given by [17, 53]

$$\dot{\mathbf{x}} = \mathbf{R}(\mathbf{\Theta})(\mathbf{v}_{r} + \mathbf{v}_{\delta}) \tag{5}$$

$$\dot{\mathbf{\Theta}} = L(\mathbf{\Theta})\boldsymbol{\omega} \tag{6}$$

$$m\dot{\mathbf{v}}_{\rm r} = m\mathbf{v}_{\rm r} \times \boldsymbol{\omega} + \mathbf{f}_{\rm net} \tag{7}$$

$$I\dot{\omega} = I\omega \times \omega + \tau_{\text{net}}$$
, (8)

where $I \in \mathbb{R}^{3\times3}$ is the inertia matrix, $f_{\text{net}} = [f_1, f_2, f_3]^T$, and $\tau_{\text{net}} = [\tau_1, \tau_2, \tau_3]^T$ are the net body-frame forces and moments acting on the vehicle, respectively.

In this work, the six degree of freedom system (5)–(8) is simplified to a three degree of freedom model of the quadrotor's longitudinal dynamics, consisting of the north-down positions $(p_{\rm N}, p_{\rm D})$ and the pitch angle θ (i.e., ignoring $p_{\rm E}$ and assuming $\psi = \phi = v_{\rm r} = p = r = 0$). The control forces acting on the quadrotor are the front thrust $0 \le T_{\rm f} \le T_{\rm max}$ and rear thrust $0 \le T_{\rm r} \le T_{\rm max}$ that are aligned with the $-\boldsymbol{b}_3$ direction where $T_{\rm max}$ is the maximum thrust. Gravity g is aligned with the \boldsymbol{i}_3 direction, and a low-speed quadratic drag acts in the direction opposite to $\boldsymbol{v}_{\rm r}$. Drag components are modeled as

$$F_{\rm D,1} = -\frac{1}{2}\rho C_{\rm D,1} A_1 || \nu_{\rm r} || u_{\rm r} \tag{9}$$

$$F_{\rm D,3} = -\frac{1}{2}\rho C_{\rm D,3} A_3 ||\nu_{\rm r}|| w_{\rm r} , \qquad (10)$$

where $||v_r||$ is the magnitude of the body-frame flow-relative velocity vector, and constants $(C_{D,1}, C_{D,3})$ and (A_1, A_3) are the coefficients of drag and the projected surface areas in the b_1 and b_3 directions, respectively. The sum of forces and moments along the body-frame axes are

$$f_1 = -mg\sin\theta + F_{D,1} \tag{11}$$

$$f_3 = mg\cos\theta + F_{D,3} - T_f - T_r$$
 (12)

$$\tau_2 = (T_f - T_r)l. \tag{13}$$

The control input is $\boldsymbol{u} = [T_f, T_r]^T$. Under the simplified dynamics (3) becomes

$$\delta_{\rm N} = \cos\theta \delta_1 + \sin\theta \delta_3 \tag{14}$$

$$\delta_{\rm D} = -\sin\theta \delta_1 + \cos\theta \delta_3 \tag{15}$$

and equations (5)–(8) simplify to:

$$\begin{bmatrix} \dot{p}_{\mathrm{N}} \\ \dot{p}_{\mathrm{D}} \\ \dot{\theta} \\ \dot{u}_{\mathrm{r}} \\ \dot{w}_{\mathrm{r}} \\ \dot{q} \end{bmatrix} = \begin{bmatrix} u_{\mathrm{r}} \cos \theta + w_{\mathrm{r}} \sin \theta + \delta_{\mathrm{N}} \\ -u_{\mathrm{r}} \sin \theta + w_{\mathrm{r}} \cos \theta \\ q \\ -qw_{\mathrm{r}} \\ qu_{\mathrm{r}} \\ 0 \end{bmatrix} + \begin{bmatrix} 0 \\ 0 \\ 0 \\ f_{1}/m \\ f_{3}/m \\ \tau_{2}/I_{22} \end{bmatrix}$$

$$(16)$$

where I_{22} is the pitch-axis mass moment of inertia of the quadrotor and the wind vertical component has been set to zero $(\delta_D = 0)$. The state vector denoting the location, pitch, and velocities of the quadrotor at a particular time instant t_k is $\mathbf{x}_k = \begin{bmatrix} p_{N,k}, p_{D,k}, \theta_k, u_{r,k}, w_{r,k}, q_k \end{bmatrix}^T$.

B. Convected Wind Model

The wind is modeled as uniform with altitude and propagating horizontally, as shown in Fig. 2. Let the wind-field in the inertial frame be denoted $\mathbf{v}_{\delta}^{I}(p_{N},t)$ where $t\geq 0$ is time. The wind-profile appears "frozen" when viewed in a translating wind frame $\mathcal{P}=\{P,p_{1},p_{2},p_{3}\}$ that initially has its origin P coinciding with the inertial frame origin P at time t=0 and moves along $-\mathbf{i}_{1}$ with a known velocity c. Let P denote the horizontal coordinate in P. The wind-field is fully specified by $\delta_{N}^{\mathcal{P}}(\beta)$ and relates to the inertial wind-field by

$$\delta_{\rm N}^{I}(p_{\rm N},t) = \delta_{\rm N}^{\varphi}(p_{\rm N}+ct) , \qquad (17)$$

where c < 0 and $\beta = p_N + ct$. This paper adopts a Gaussian process (GP) model for $\delta_N^{\mathcal{P}}(\beta)$; however, in principle, other wind profiles $\delta_N^{\mathcal{P}}(\beta)$ can be estimated using GP regression.

The wind profile is a scalar, one-dimensional GP, $\delta_{N}^{\mathcal{P}}(\beta)$, which is a random function of an argument $\beta \in \mathbb{R}$ representing the horizontal position relative to the origin of the wind frame \mathcal{P} . The GP is completely specified by its mean function $\mu(\beta)$ over the input space and covariance function $\kappa(\beta, \beta')$ (also called the *kernel*).

$$\mu(\beta) = \mathbb{E}[\delta_{N}^{\mathcal{P}}(\beta)] \tag{18}$$

$$\kappa(\beta, \beta') = \mathbb{E}[\{\delta_{N}^{\mathcal{P}}(\beta) - \mu(\beta)\}\{\delta_{N}^{\mathcal{P}}(\beta') - \mu(\beta)'\}\}], \tag{19}$$

where $\mathbb{E}[\cdot]$ is the expected value operator. This work considers the squared exponential kernel

$$\kappa(h; \boldsymbol{\theta}) = \sigma^2 \exp\left(-\frac{h^2}{2L^2}\right),\tag{20}$$

where $h = \beta - \beta'$ is the spatial lag term, and $\theta = [L, \sigma]^T$ is a vector of hyperparameters where L is the length scale of the GP and σ^2 is the variance. The mean $\mu(\beta)$ is assumed to be constant. The length scale relates to the smoothness of the wind-field over the spatial coordinate β (i.e., gust duration), whereas the variance relates to the amplitude of peaks and troughs (i.e., gust magnitude). A realization of a GP can be generated, for example, by drawing a Gaussian random

vector (representing the value of the realization over a grid of points) from a mean and covariance matrix defined according to (18)–(19). In this work, realizations of the GP wind-profile are generated for uniformly spaced grid points over a distance $\lambda = d + ct_m$, where d is the horizontal region within which the quadrotor and anemometers operate, and t_m is an upper bound on the total anticipated sensing and takeoff duration. The span λ allows for the profile to be well-defined within the operating region for all $t \in [0, t_m]$.

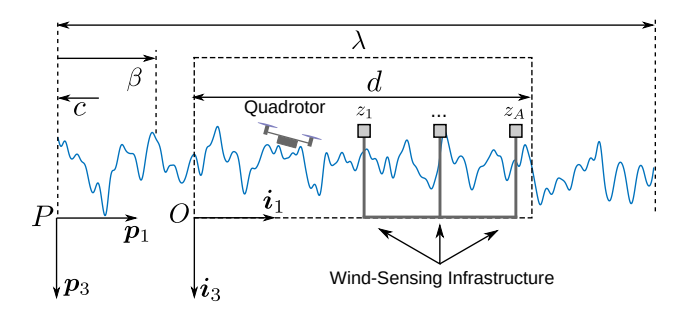


Fig. 2 Wind-field model where coordinate β represents the distance from the origin P in the wind frame, c is the wind propagation speed at which the origin P moves to the left, and d is the operating region of the quadrotor. The wind-profile used for simulation (and estimation) has length $\lambda = d + ct_m$, and the horizontal coordinate $\beta \in [0, \lambda]$ is the distance from P in the p_1 direction.

C. Wind Sensing Infrastructure

The operating environment of the quadrotors is instrumented with a total of A networked wind-sensing instruments (anemometers) that are positioned upstream of the quadrotor takeoff position at fixed locations z_i for i = 1, ..., A, measured as the horizontal distance from O. An anemometer located at position z_i measures

$$y_i(t_k) = \delta_N^I(z_i, t_k) + \epsilon \tag{21}$$

at time t_k , where $\epsilon \sim \mathcal{N}(0, \sigma_n^2)$ is zero-mean, Gaussian measurement noise with variance σ_n^2 and $\delta_N^I(z_i, t_k)$ is obtained from (17) assuming a wind profile $\delta_N^{\mathcal{P}}$. Define the vector of measurements taken by all anemometers at a discrete-time instant t_k as $\mathbf{y}_k = [y_1, \dots, y_A]^T$. Similarly, define the vector of positions of the anemometers for each set of measurements as $\mathbf{s}_k = [z_1, \dots, z_A]^T$. Let F be the sampling rate (Hz) of the sensors so that for consecutive sample times $t_k - t_{k-1} = (1/F)$. Prior to takeoff, the anemometers collect data for a total of t_N seconds as represented by the matrix

$$\mathbf{Y} = \begin{bmatrix} t_1 & t_2 & \cdots & t_N \\ s_1 & s_2 & \cdots & s_N \\ \mathbf{y}_1 & \mathbf{y}_2 & \cdots & \mathbf{y}_N \end{bmatrix}^T \in \mathbb{R}^{(2A+1)\times N} , \qquad (22)$$

where t_1, \ldots, t_N are the times at which measurements are taken. The information gathered by the anemometers preceding takeoff is made available to a centralized planner for wind estimation and trajectory planning.

D. Problem Statement

The objective is to plan a minimum-time trajectory to a desired position $(p_{N,\text{final}}, p_{D,\text{final}})$ for a quadrotor that has access to nearby wind sensing infrastructure in an uncertain wind-field. Let $t_{\text{init}} \ge t_N$ be the takeoff time of the quadrotor and t_{final} be the final time that the quadrotor reaches the desired position. The optimal control problem is to

minimize
$$J(\boldsymbol{u}(\cdot)) = \int_{t_{\text{init}}}^{t_{\text{final}}} dt = t_{\text{final}} - t_{\text{init}}$$
 (23)

subject to the boundary conditions

$$p_{N}(t_{\text{init}}) = p_{N,\text{init}} \qquad p_{N}(t_{\text{final}}) = p_{N,\text{final}}$$

$$p_{D}(t_{\text{init}}) = p_{D,\text{init}} \qquad p_{D}(t_{\text{final}}) = p_{D,\text{final}}$$

$$\theta(t_{\text{init}}) = 0 \qquad \theta_{\text{min}} \leq \theta(t_{\text{final}}) \leq \theta_{\text{max}}$$

$$u_{r}(t_{\text{init}}) = 0 \qquad u_{r,\text{min}} \leq u_{r}(t_{\text{final}}) \leq u_{r,\text{max}}$$

$$w_{r}(t_{\text{init}}) = 0 \qquad w_{r,\text{min}} \leq w_{r}(t_{\text{final}}) \leq w_{r,\text{max}}$$

$$q(t_{\text{init}}) = 0 \qquad q_{\text{min}} \leq q(t_{\text{final}}) \leq q_{\text{max}}$$

$$(24)$$

the dynamics (16) and the control constraints $0 \le T_f, T_r \le T_{\text{max}}$. The term δ_N appearing in the dynamics (16) is not known and is estimated using available data (22). The terminal boundary conditions include a specific waypoint in the vertical plane $(p_{N,\text{final}}, p_{D,\text{final}})$ and inequality constraints for the minimum and maximum pitch angle, wind-relative velocities, and pitch rate.

IV. Wind Estimation and Trajectory Planning

This section proposes a GP-based wind estimation procedure for the convected wind-field model and describes how the wind-estimate is used to formulate the minimum-time trajectory planning problem to be solved numerically.

A. Gaussian Process Wind-field Regression

The raw data collected by the wind-sensing infrastructure is encapsulated in the matrix Y (22). The measurements are collected at sampling locations z_i at times t_i for i = 1, ..., N. However, since the wind-field is convected at speed c the measurement locations in the wind frame are

$$\beta_i = z_i - ct_i \ . \tag{25}$$

The wind estimation approach is based on ordinary Kriging, which is a form of GP regression that handles GP process models with an unknown constant mean. Given a set of M observations of the wind-field, $f = [y_1^T, \ldots, y_M^T]^T$ at wind-frame locations $\boldsymbol{\beta} = [\beta_1, \ldots, \beta_M]^T$ the ordinary Kriging estimator [54, Ch. 4] predicts the estimate of the wind $\hat{\delta}_N^{\mathcal{P}}(\boldsymbol{g}; \boldsymbol{Y})$ at a vector of grid points $\boldsymbol{g} = [g_1, \ldots, g_G]^T$ along with the corresponding covariance matrix $\boldsymbol{P}_{\delta_N}(\boldsymbol{g}; \boldsymbol{Y}) \in \mathbb{R}^{G \times G}$. The prediction is computed according to

$$\hat{\delta}_{N}^{\mathcal{P}}(\boldsymbol{g};\boldsymbol{Y}) = \begin{bmatrix} \boldsymbol{f}^{T} & 0 \end{bmatrix} \boldsymbol{K}(\boldsymbol{\beta},\boldsymbol{\beta})^{-1} \boldsymbol{K}(\boldsymbol{g},\boldsymbol{\beta})$$
(26)

$$\boldsymbol{P}_{\delta_{N}}(\boldsymbol{g};\boldsymbol{Y}) = \boldsymbol{K}(\boldsymbol{g},\boldsymbol{g}) - \boldsymbol{K}(\boldsymbol{g},\boldsymbol{\beta})\boldsymbol{K}(\boldsymbol{\beta},\boldsymbol{\beta})^{-1}\boldsymbol{K}(\boldsymbol{g},\boldsymbol{\beta})^{\mathrm{T}}, \qquad (27)$$

where $K(\beta, \beta)$ is a $(M+1) \times (M+1)$ matrix relating the covariance of observation points to each other,

$$\boldsymbol{K}(\boldsymbol{s},\boldsymbol{s}) = \begin{bmatrix} \kappa(\beta_1,\beta_1) & \cdots & \kappa(\beta_1,\beta_M) & 1 \\ \vdots & \ddots & \vdots & \vdots \\ \kappa(\beta_M,\beta_1) & \cdots & \kappa(\beta_M,\beta_M) & 1 \\ 1 & \cdots & 1 & 0 \end{bmatrix},$$
(28)

K(g, g) is a $G \times G$ matrix relating the covariance of grid points g to each other, i.e., the *i*th row and *j*th column is given by $[K(g, g)]_{ij} = \kappa(g_i, g_j)$ from (20), and $K(g, \beta)$ is the $G \times M$ matrix relating the covariance of grid points to samples. The data matrix Y is included as a parameter in the expressions (26)–(27) to emphasize that the spatial locations β and observations f are derived from Y using (25).

The GP estimate (26) is computed in the wind-frame using available data just before takeoff (i.e., up to time t_N) at the grid points g. The estimate in the \mathcal{P} frame is converted into a time-varying estimate in the I frame via the relationship (17). That is, the wind-frame grid points g are shifted to inertial-frame points g + ct

$$\hat{\delta}_{N}^{I}(t, \boldsymbol{g} + ct; \boldsymbol{Y}) = \hat{\delta}_{N}^{\mathcal{P}}(\boldsymbol{g}; \boldsymbol{Y}) , \qquad (29)$$

where the (\cdot) indicates an estimate, the term ct is added element-wise to the vector g. The grid points g are uniformly spaced over the interval $[0, \lambda]$, and linear interpolation is used to determine the estimated wind magnitude in-between

grid points. To account for the measurement noise (21) the kernel function $\kappa(\beta, \beta')$ is modified by adding σ_n^2 to the expression in (20) in cases where $\beta = \beta'$. The GP regression in this work makes the simplifying assumption that the location of each measurement is known precisely and the hyperparameters of the wind GP are known a priori. However, the approach can be extended to incorporate localization uncertainty [55] and to learn hyperparameters in real-time [56].

To reduce computational complexity during GP regression a spatiotemporal truncation strategy may be employed [57]. Let $\varphi(t) = [-ct - \eta L, c(t_m - t) + d + \eta L]$ denote a time-dependent spatial zone of acceptance in the wind-frame where measurements are included for regression with $\eta > 0$ being a chosen parameter. Measurements separated by three or more length scales have little influence on the estimates and thus $\eta \geq 3$ or greater is suggested. Only measurements associated with locations $\beta_i \in \varphi(t_N)$ are used for GP regression.

B. Wind Regression Example

To illustrate the GP regression with the convencted wind-field model, an example GP wind profile was generated in frame \mathcal{P} using a mean $\mu_w=8$ m/s, a GP length scale L=1.5 m, and a GP variance $\sigma^2=4$ m². The generated wind-field was then propagated through the simulated environment at a speed c, as described in Sec. III.B. Noisy measurements were taken by three stationary anemometers at a sampling frequency of 10 Hz with measurement noise $\sigma_n^2=0.6$ (m/s)². Once the first measurement reaches the initial position of the quadrotor, the trajectory planner uses the data collected for planning. The anemometers in the environment are denoted by the different colored square markers, and their respective measurements are shown by the same-colored star markers that propagate with the wind over time. Samples were taken from 0 seconds to $t_N=5$ seconds. Three snapshots at 2, 8, and 14 seconds into the simulation are shown.

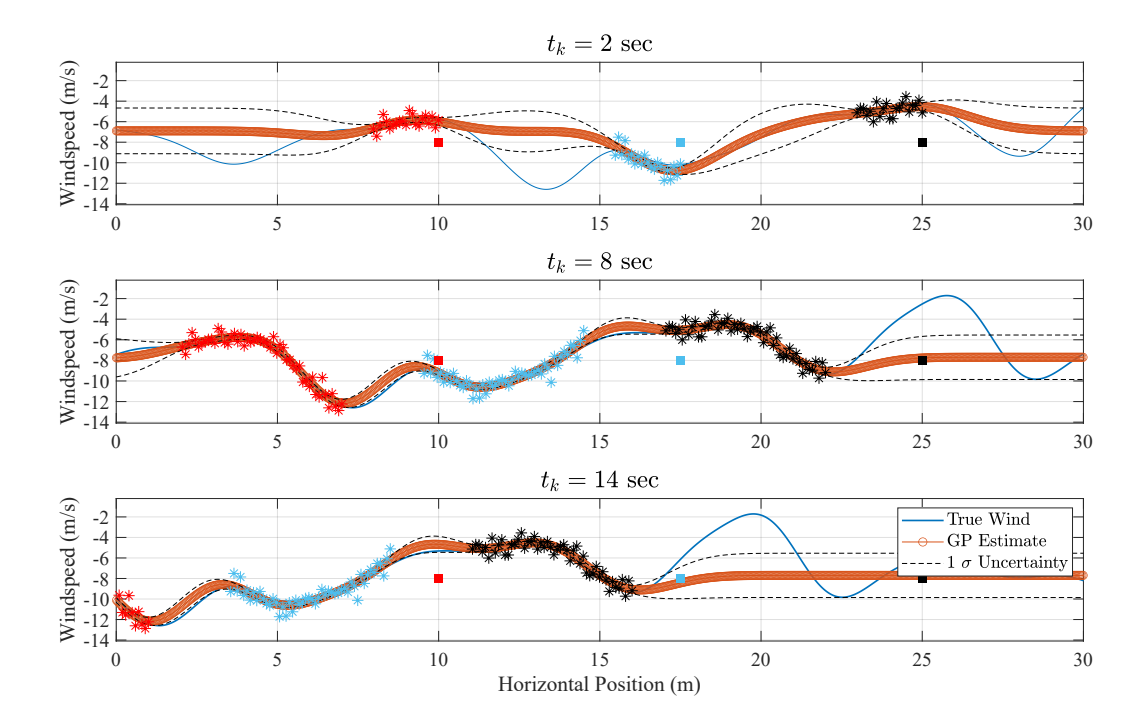


Fig. 3 Example of the wind-field estimate evolving over the operating environment for three snapshots in time, with GP length scale L=1.5 m, and GP variance $\sigma=4$ (m/s)². The red, blue, and black squares represent the anemometers in the environment, and their respective measurements are shown as stars in the same colors (at a sampling frequency of 10 Hz with measurement noise $\sigma_n^2=0.6$ (m/s)²). The final estimate is made at time $t_N=5$ sec. and for times $t>t_N$ the estimated wind-profile is convected downstream.

C. Proposed Estimation and Trajectory Planning Framework

To address the time-optimal control problem of Sec. III.D, the estimation and trajectory planning framework sketched in Fig. 4 is proposed.

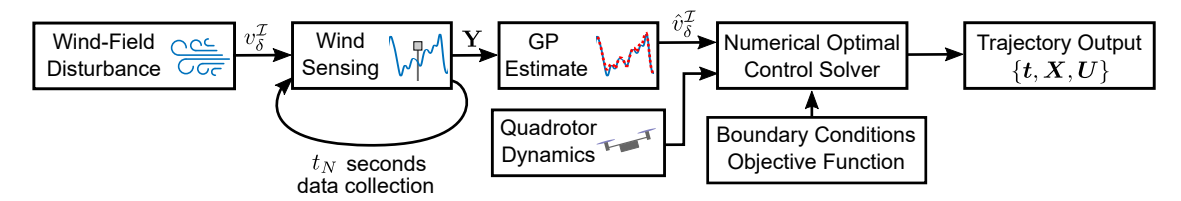


Fig. 4 Proposed framework for leveraging wind-sensing infrastructure in an optimal control solver to plan a time-optimal trajectory to reach a desired waypoint.

A quadrotor is initialized in an environment with a wind-field disturbance, and with A anemometers representing nearby wind sensing infrastructure that is available to the quadrotor. The anemometers sampled the wind-field for t_N seconds, as detailed in Sec. III.C. These measurements are used to generate a wind-field estimate, using the approach of Sec. IV.A which is provided to an optimal control solver. The modified quadrotor dynamics are

$$\begin{bmatrix} \dot{p}_{\mathrm{N}} \\ \dot{p}_{\mathrm{D}} \\ \dot{\theta} \\ \dot{u}_{\mathrm{r}} \\ \dot{w}_{\mathrm{r}} \\ \dot{q} \end{bmatrix} = \begin{bmatrix} u_{\mathrm{r}} \cos \theta + w_{\mathrm{r}} \sin \theta + \hat{\delta}_{\mathrm{N}}(t, p_{\mathrm{N}}) \\ -u_{\mathrm{r}} \sin \theta + w_{\mathrm{r}} \cos \theta \\ q \\ -qw_{\mathrm{r}} \\ qu_{\mathrm{r}} \\ 0 \end{bmatrix} + \begin{bmatrix} 0 \\ 0 \\ 0 \\ f_{1}/m \\ f_{3}/m \\ \tau_{2}/I_{22} \end{bmatrix}$$

$$(30)$$

where $\hat{\delta}_{N}(t_{k}, p_{N,k})$ is the wind-field estimate sampled at the current position of the quadrotor $p_{N,k}$ (using linear interpolation over that grid points in (29)). The dynamics (30) model the wind-field as a know time-varying disturbance for the purposes of trajectory planning. The trajectory planning uses the numerical optimal control solver GPOPS-II [52], as described next.

V. Simulation Results

This section discusses the setup of several illustrative examples used to demonstrate the approach, implementation of the proposed framework of Sec. IV.C in the numerical optimal control solver GPOPS-II [52], and discusses the results of the simulation trials comparing performance under different wind conditions and sensing characteristics.

A. Simulation Setup

To evaluate the framework proposed in Sec. IV.C using GPOPS-II in MATLAB, six simulations were conducted that varied the wind mean (μ_w) , GP variance (σ^2) , GP length scale (L), anemometer measurement noise (σ_n^2) , and anemometer measurement frequency (F), as shown in Table 1. For each set of simulation parameters, a GP wind-field was generated by specifying G uniformly spaced grid points $\mathbf{g} \in [0, \lambda]$ and hyperparameters $\mathbf{\theta} = [L, \sigma]^T$.

Table 1 Table of simulation trials used to evaluate the proposed estimation and trajectory planning framework.

Trial	Wind mean, μ_W	GP var., σ^2	GP scale, L	Sensor noise, σ_n^2	Sensor freq., F	Wind Intensity / Sensor Quality
1	4 m/s	$(\mu_w/4) \text{ m}^2$	$(c t_m/10) \text{ m}$	$0.6 (\text{m/s})^2$	10 Hz	Low wind / higher-quality sensor
2	4 m/s	$(\mu_w/4) \text{ m}^2$	$(c t_m/10) \text{ m}$	$1.2 (\text{m/s})^2$	2 Hz	Low wind / lower-quality sensor
3	8 m/s	$(\mu_w/2) \text{ m}^2$	$(c t_m/20)$ m	$0.6 (\text{m/s})^2$	10 Hz	Moderate wind / higher-quality sensor
4	8 m/s	$(\mu_w/2) \text{ m}^2$	$(c t_m/20)$ m	$1.2 (\text{m/s})^2$	2 Hz	Moderate wind / lower-quality sensor
5	12 m/s	$(\mu_w/2) \text{ m}^2$	$(c t_m/20)$ m	$0.6 (\text{m/s})^2$	10 Hz	High wind / higher-quality sensor
6	12 m/s	$(\mu_w/2) \text{ m}^2$	$(c t_m/20) \text{ m}$	1.2 (m/s)^2	2 Hz	High wind / lower-quality sensor

Three anemometers were initialized at equal distances in the operating region, upstream of the initial location of the quadrotor. At the start of the simulation (t = 0), the anemometers begin sampling the wind-field. The first measurement reaches the quadrotor's initial position after $t_N = t_{\text{init}} = (z_1 - p_{\text{N,init}})/|c|$ seconds. At this time a GP estimate is computed and a trajectory is planned.

B. Implementation in GPOPS-II

GPOPS-II is an hp-adaptive version of the Legendre-Gauss-Radau (LGR) orthogonal collocation method, which uses Gaussian quadrature implicit integration with collocation performed at LGR points. This process involves defining the upper and lower limits of the state, time, and control of the optimal control problem, the objective function, and the dynamics, then meshing a solution to the objective between the initial and final conditions using LGR orthogonal collocation. Detailed information on the setup and use of GPOPS-II can be found in [52, 58]. Here we briefly discuss the general parameters used for the presented simulation results. For this work, we use a mesh tolerance of 1×10^{-7} , and set the maximum number of iterations to 5. Simulations were conducted using the following boundary conditions:

$$\begin{aligned} p_{\rm N}(t_{\rm init}) &= 5 \text{ m} & p_{\rm N}(t_{\rm final}) &= 15 \text{ m} \\ p_{\rm D}(t_{\rm init}) &= 0 \text{ m} & p_{\rm D}(t_{\rm final}) &= -5 \text{ m} \\ \theta(t_{\rm init}) &= 0^{\circ} & -30^{\circ} \leq \theta(t_{\rm final}) \leq 30^{\circ} \\ u_{\rm r}(t_{\rm init}) &= 0 \text{ m/s} & -5 \text{ m/s} \leq u_{\rm r}(t_{\rm final}) \leq 5 \text{ m/s} \\ w_{\rm r}(t_{\rm init}) &= 0 \text{ m/s} & -5 \text{ m/s} \leq w_{\rm r}(t_{\rm final}) \leq 5 \text{ m/s} \\ q(t_{\rm init}) &= 0^{\circ}/\text{s} & -100^{\circ}/\text{s} \leq q(t_{\rm final}) \leq 100^{\circ}/\text{s} \end{aligned}$$
(31)

along with an initial time of $t_{\text{init}} = 5$ sec. The final time was bounded as $t_{\text{init}} \le t_{\text{final}} \le 30$ sec., and the state was conservatively bounded according to

$$-50 \text{ m} \le p_{\text{N}}(t) \le 50 \text{ m}$$
 (32)

$$-50 \text{ m} \le p_{D}(t) \le 50 \text{ m} \tag{33}$$

$$-60^{\circ} \le \theta(t) \le 60^{\circ} \tag{34}$$

$$-50 \text{ m/s} \le u_{\rm r}(t) \le 50 \text{ m/s} \tag{35}$$

$$-50 \text{ m/s} \le w_{\rm r}(t) \le 50 \text{ m/s} \tag{36}$$

$$-1000^{\circ}/s \le q(t) \le 1000^{\circ}/s \tag{37}$$

for all $t \in (t_{\text{init}}, t_{\text{final}})$. The front/rear thrust values were bounded as $0 \le T_{\text{f}}, T_{\text{r}} \le T_{\text{max}}$. All trials detailed in Table 1 were simulated for a single quadrotor with parameters listed in Table 2. Three anemometers were initialized to positions located at $z_{1,2,3} = \{10, 17.5, 25\}$ m. GPOPS-II returns a planned trajectory $\{t, X, U\}$, where t is a time vector spanning from the take-off time to the final time, X is a matrix containing the corresponding state history, and U is the control history used over the time span t to achieve X.

To verify the results of GPOPS-II solutions, the dynamics were re-simulated with explicit Runge-Kutta numerical integration (i.e., ODE45 in MATLAB [59]), the known initial condition, the same estimated wind-field used in (30), and spline interpolation across the control history U and times t. While in many cases, the output trajectory could be reproduced fairly accurately, we also encountered instances where significant discrepancies occurred. These discrepancies may perhaps be attributed to interpolation or integration differences between ODE45 and GPOPS-II. In this paper, only verified results are reported for which the ODE45 simulation closely matches the GPOPS-II trajectory (i.e., with the final state of both simulations reaching within 2% of the desired waypoint when simulated with the same estimated wind conditions). Once a solution was verified, the dynamics were again re-simulated in ODE45 using the true wind-field as the disturbance. The output of this latter simulation is referred to as the actual trajectory.

Table 2 Parameters used in simulations. The horizontal line separates vehicle dynamics parameters and wind-field model and estimation parameters.

Parameter	Symbol	Value
Quadrotor mass	m	3.696 kg
Drag coefficients	$(C_{D,1}, C_{D,2})$	(0.8, 0.4)
Surface areas	(A_1, A_3)	$(0.0279, 0.109) \text{ m}^2$
Max. thrust bound	$T_{ m max}$	41.6964 N
Air density	ρ	1.293 kg/m^3
Inertia	I_{22}	0.0292 kg·m ²
Distance between propellers	1	0.254 m
Operating region length	d	40 m
Number of grid points	G	2000
Truncation parameter	η	7
Wind profile propagation speed	c	−1 m/s
Number of anemometers	A	3

C. Results and Discussion

The state and control history generated by GPOPS-II (i.e., the planned trajectory assuming the estimated wind-field) for each trial in Table 1 are presented alongside simulation of the control history with ODE45 using the true wind-field (i.e., the actual trajectory). The trajectory elapsed time $(t_{\text{final}} - t_{\text{init}})$ and the final Euclidean distance error between the planned and actual trajectories are reported.

1. Trial 1: Low Wind Intensity, Higher-Quality Wind Sensor

The results for Trial 1 are shown in Fig. 5. Since the quadrotor is initialized with zero velocity, pitch, and pitch rate, it is significantly perturbed when it encounters the wind disturbance on takeoff during the initial moments of the simulation. As can be seen in the plot of pitch angle over time the quadrotor initially pitches to its minimum allowable value (-60°) — holds this configuration while applying full thrust — and then transitions to a maximum allowable pitch angle (60°) just before levelling off as the terminal state is reached. The thrust controls vary rapidly during pitch change events, such as at 5.1 seconds, 6.1 seconds, and 6.8 seconds, with the pitch-rate saturating to the maximum allowable value $(\pm 1000^{\circ}/s)$ during these times. This qualitative behavior of the controls and state history is similar across all trials. In this trial, with low wind and low sensor noise, the actual trajectory closely matches the planned trajectory and the final Euclidean distance error between them was 0.2259 m. The planned trajectory cost was $(t_{\rm final} - t_{\rm init}) = 1.8254$ seconds.

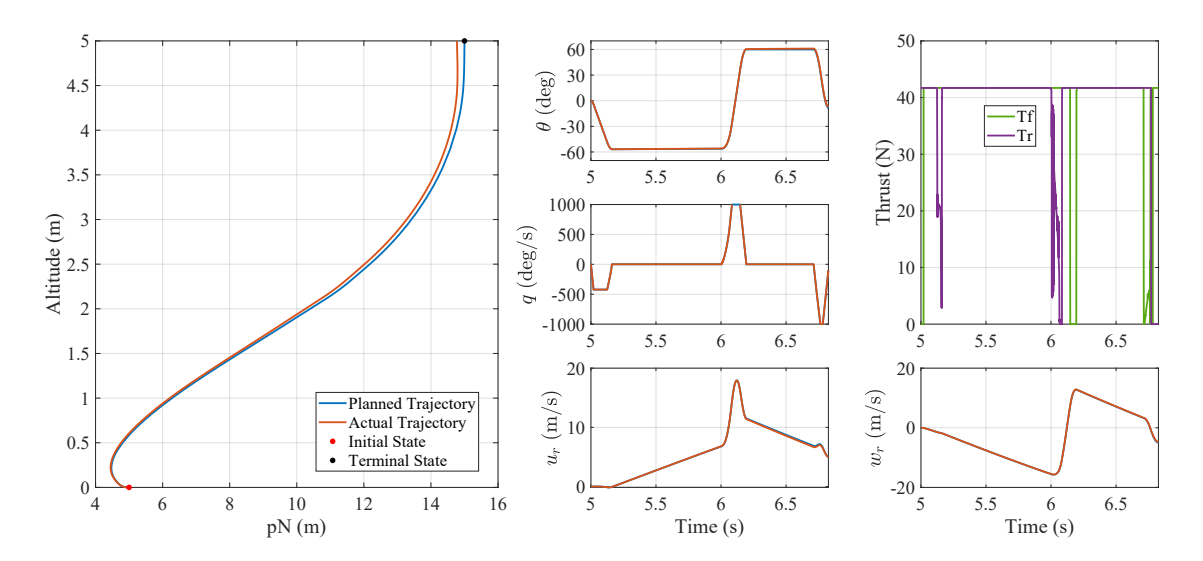


Fig. 5 Simulation results for Trial 1. The left panel depicts the actual and planned trajectories in the vertical plane. The middle three, and bottom right panels show the pitch angle, pitch rate, and u_r , w_r flow-relative velocities, respectively. The upper right panel illustrates the control generated by GPOPS-II.

2. Trial 2: Low Wind Intensity, Lower-Quality Wind Sensor

In Trial 2 (see Fig. 6) the measurement noise was increased, and the sampling frequency was decreased compared to Trial 1. This trial simulates the effects of using a lower-quality wind sensor while holding the wind-field hyperparameters constant. The overall trajectory is similar to Trial 1 and the final Euclidean distance error between the actual/planned trajectories at the final time is 0.0120 m (less than but comparable to Trial 1). The planned trajectory cost was $(t_{\text{final}} - t_{\text{init}}) = 1.6824$ seconds. This result suggests that with a relatively low wind disturbance magnitude, the quadrotor was not adversely affected by a reduced measurement quality. The reduction in position error compared to Trial 1 is counter-intuitive, but it may be attributed to differences in numerical integration (especially over the rapidly changing control during pitch maneuvers).

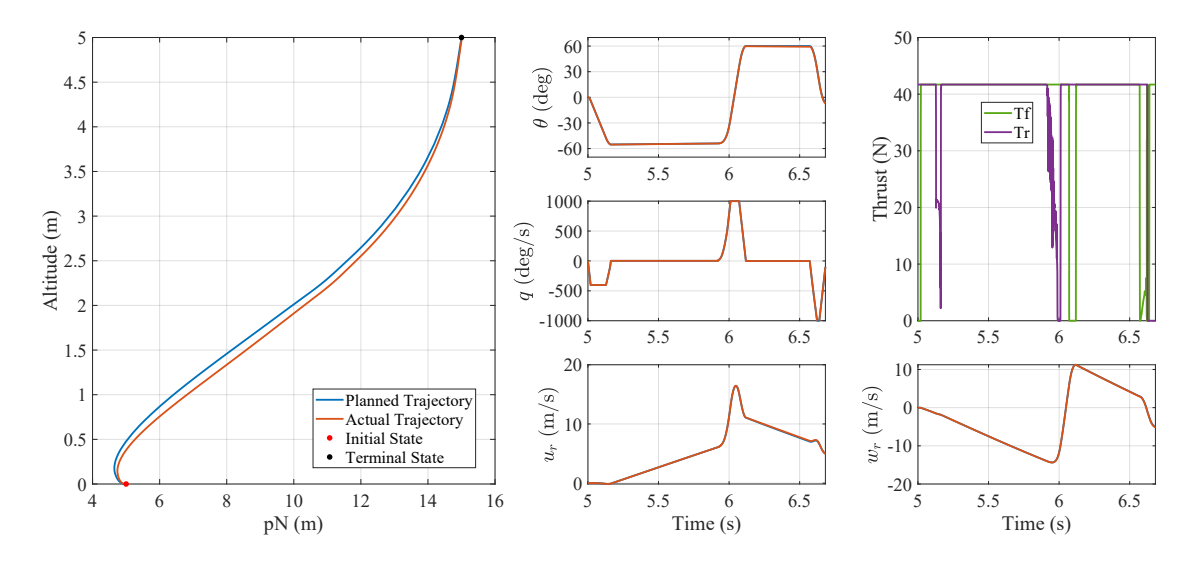


Fig. 6 Simulation results for Trial 2. The left panel depicts the actual and planned trajectories in the vertical plane. The middle three, and bottom right panels show the pitch angle, pitch rate, and u_r , w_r flow-relative velocities, respectively. The upper right panel illustrates the control generated by GPOPS-II.

3. Trial 3: Medium Wind Intensity, Higher-Quality Wind Sensor

In Trial 3 (see Fig. 7) the wind mean was increased compared to Trials 1 and 2, with the same GP hyperparameters as used in Trial 1. This change resulted in stronger wind disturbance with more sudden gusts. Fig. 3 shows a realization of the GP wind-field for Trials 3 and 4 using the same parameters. The measurement characteristics used in Trial 3 were also the same as those in Trial 1. The final Euclidean distance error between the planned and actual trajectories was 1.1611 m. The planned trajectory cost was $(t_{\text{final}} - t_{\text{init}}) = 2.5405$ seconds. In Trial 3, the actual trajectory is affected more greatly than that of Trial 1. For a wind-field with a greater mean, small errors in the estimated wind result amplified path deviations in the actual trajectory.

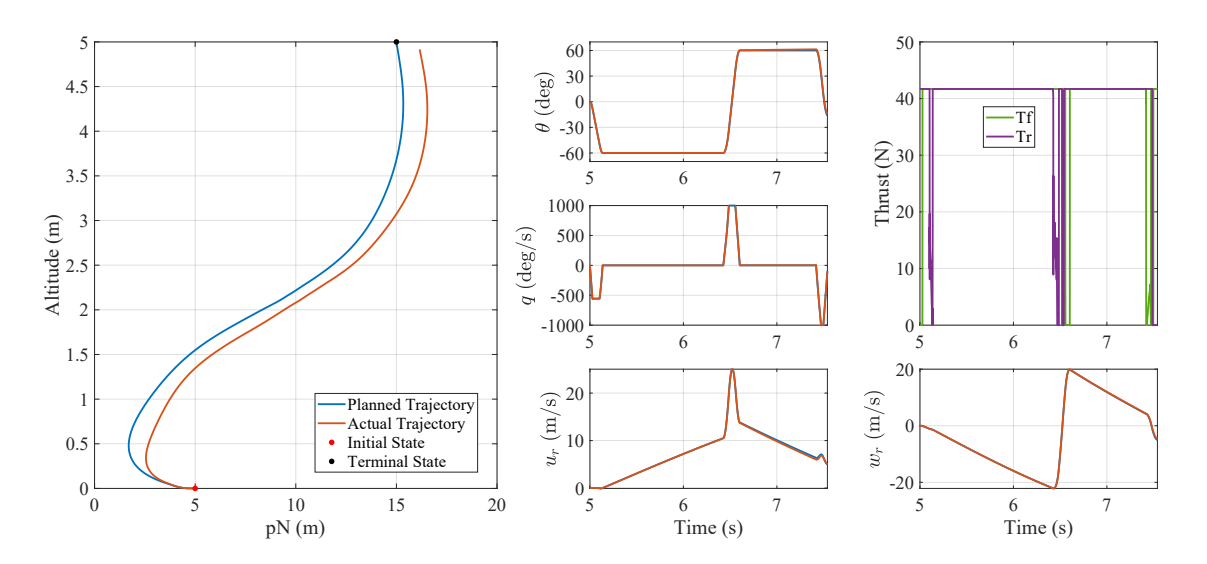


Fig. 7 Simulation results for Trial 3. The left panel depicts the actual and planned trajectories in the vertical plane. The middle three, and bottom right panels show the pitch angle, pitch rate, and u_r , w_r flow-relative velocities, respectively. The upper right panel illustrates the control generated by GPOPS-II.

4. Trial 4: Medium Wind Intensity, Lower-Quality Wind Sensor

Trial 4 used the same moderate wind characteristics as Trial 3, but the lower-quality wind sensor. The Euclidean position error for this trial (0.7894 m, see Fig. 8) is comparable to Trial 3. The planned trajectory cost was $(t_{\text{final}} - t_{\text{init}}) = 2.3542$ seconds. In comparison to the earlier Trials 1 and 2 at the lower mean wind setting, the results for Trials 3 and 4 in moderate wind approximately double the position error at the terminal state. Statistical analysis over a larger number of trials and refinement of the numerical integration strategy used in evaluating the actual versus planned trajectories would allow characterizing the effect of sensor quality in the low-to-moderate wind cases.

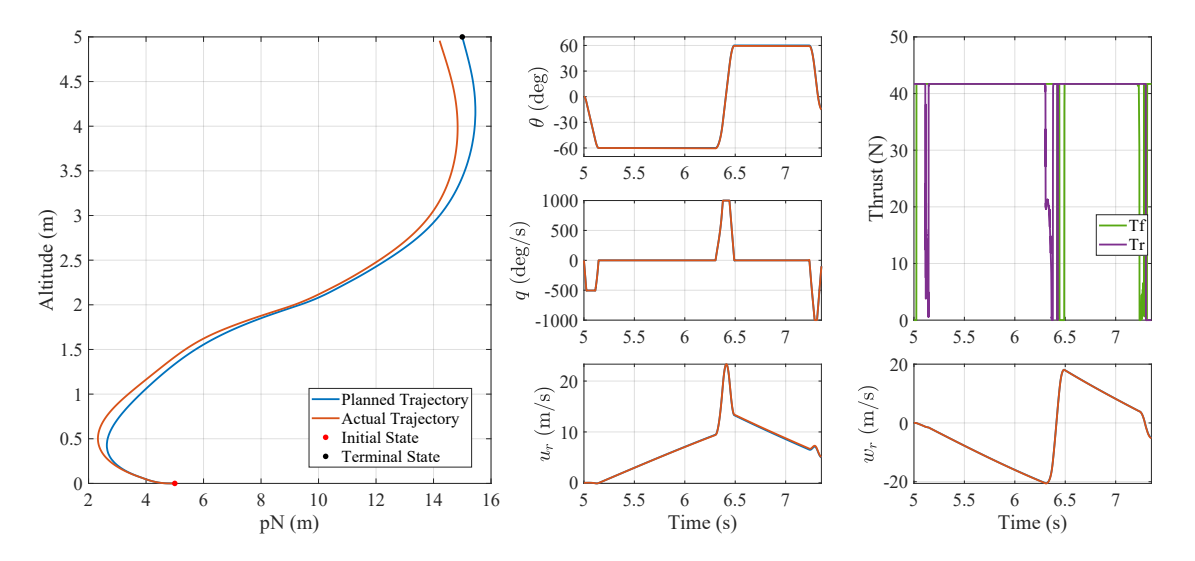


Fig. 8 Simulation results for Trial 4. The left panel depicts the actual and planned trajectories in the vertical plane. The middle three, and bottom right panels show the pitch angle, pitch rate, and u_r , w_r flow-relative velocities, respectively. The upper right panel illustrates the control generated by GPOPS-II.

5. Trial 5: High Wind Intensity, Higher-Quality Wind Sensor

Similar to Trials 1 and 3, Trial 5 evaluates higher-quality sensing but with a stronger wind than previously simulated. The final Euclidean distance error was 1.0850 m, larger than most of the previous cases, and still reasonably close the the desired waypoint. The planned trajectory cost was $(t_{\text{final}} - t_{\text{init}}) = 3.105$ seconds.

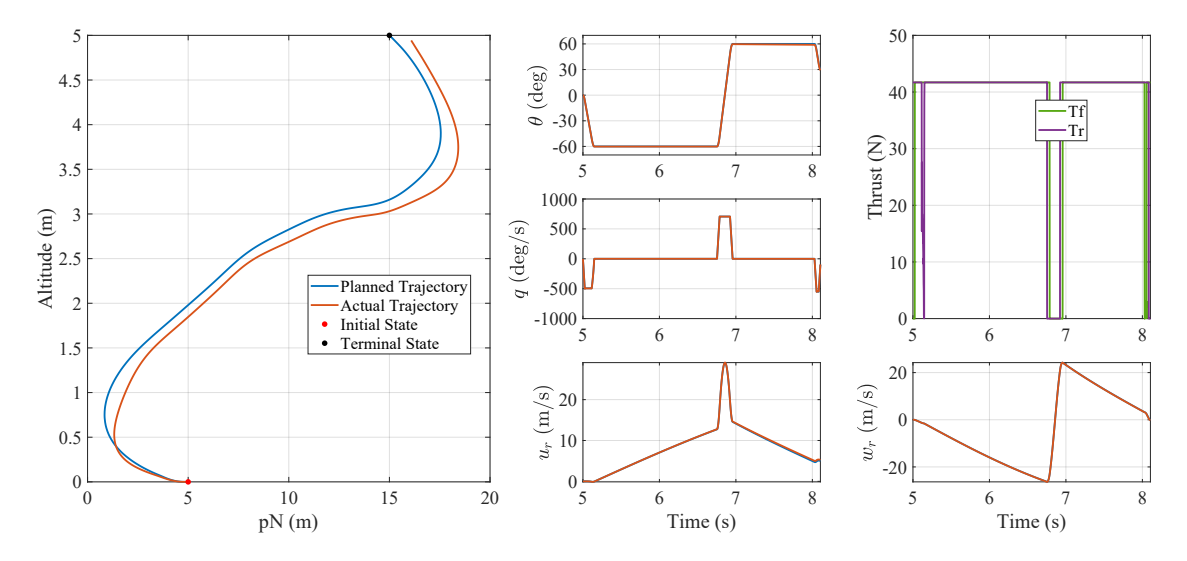


Fig. 9 Simulation results for Trial 5. The left panel depicts the actual and planned trajectories in the vertical plane. The middle three, and bottom right panels show the pitch angle, pitch rate, and u_r , w_r flow-relative velocities, respectively. The upper right panel illustrates the control generated by GPOPS-II.

6. Trial 6: High Wind Intensity, Lower-Quality Wind Sensor

Lastly, Trial 6 evaluates a similar wind condition to Trial 5 but with a lower-quality wind sensor. The final Euclidean distance error between the planned and actual trajectories was 4.6731 m — the largest of all simulations presented

and more than four times the error for Trial 5. For this strongest wind case, the wind sensor quality has a significant affect on position error. The planned trajectory cost was $(t_{\text{final}} - t_{\text{init}}) = 2.8504$ seconds. The lower cost of the trajectory for the case of a lower-quality wind sensor (compared to Trial 5) may be attributed to the decreased accuracy of the wind-field estimate.

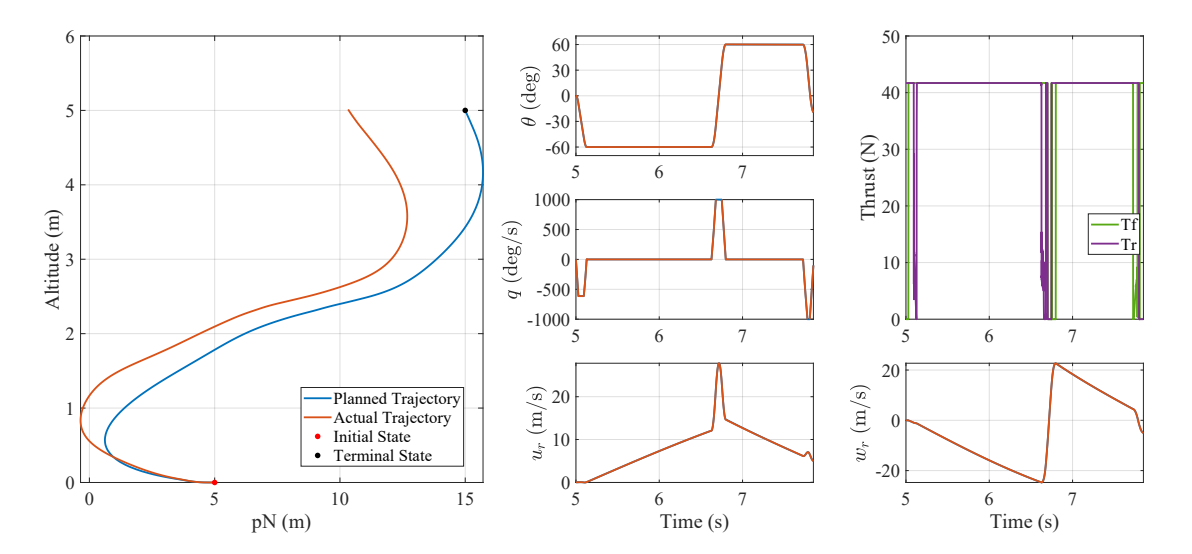


Fig. 10 Simulation results for Trial 6. The left panel depicts the actual and planned trajectories in the vertical plane. The middle three, and bottom right panels show the pitch angle, pitch rate, and u_r , w_r flow-relative velocities, respectively. The upper right panel illustrates the control generated by GPOPS-II.

VI. Conclusion and Future Work

An estimation and control framework was presented that supports trajectory planning in a one-dimensional uncertain wind-field. The wind-field magnitude was modeled as a Gaussian Process (GP) that is spatially varying, with an unknown mean, and is convected downstream at a known constant speed. Wind-sensing infrastructure in the operating area provides noisy measurements of the wind at upstream locations and is assimilated using Gaussian process regression to estimate the wind-field at unsampled locations and future time instants. The resulting GP estimate is used by a numerical optimal control solver (GPOPS-II) to compute a minimum-time trajectory to a desired vertical-plane position. The approach was evaluated over six trials that varied mean wind strength, wind strength variance, and wind-sensing measurement frequency and noise. The trials simulated the quadrotor following the optimized control in an open-loop fashion in the actual (true) wind field. Simulation results showed that the proposed approach is able to compensate for the wind-field in the operating environment and reach the desired waypoint reasonable well. The position error to the desired waypoint at the terminal time increased in the trials where the wind magnitude was larger (8 and 12 m/s) compared to those where the wind magnitude was smaller (4 m/s). For the highest wind case, increasing measurement noise and reducing the sampling frequency led to lower quality wind estimate that decreased performance.

Future work may consider more realistic wind-field models (e.g., extending to three-dimensions, consider an unknown convection speed) and other control objectives (e.g., trajectory tracking). The approach could also be combined with wind-aware feedback-control strategies and multi-vehicle cooperative estimation and control.

Acknowledgments

This work was supported by NSF Grant No. 2301475.

References

[1] Giersch, S., El Guernaoui, O., Raasch, S., Sauer, M., and Palomar, M., "Atmospheric flow simulation strategies to assess turbulent wind conditions for safe drone operations in urban environments," *Journal of Wind Engineering and Industrial*

- Aerodynamics, Vol. 229, No. October, 2022, pp. 1–20. https://doi.org/10.1016/j.jweia.2022.105136.
- [2] Mohamed, A., Marino, M., Watkins, S., Jaworski, J., and Jones, A., "Gusts encountered by flying vehicles in proximity to Buildings," *Drones*, Vol. 7, No. 1, 2023, pp. 22–48. https://doi.org/10.3390/drones7010022.
- [3] Alexis, K., Papachristos, C., Siegwart, R., and Tzes, A., "Robust model predictive flight control of unmanned rotorcrafts," *Journal of Intelligent & Robotic Systems*, Vol. 81, No. 3, 2016, pp. 443–469. https://doi.org/10.1007/s10846-015-0238-7.
- [4] Craig, W., Yeo, D., and Paley, D. A., "Geometric attitude and position control of a quadrotor in wind," *Journal of Guidance, Control, and Dynamics*, Vol. 43, No. 5, 2020, pp. 870–883. https://doi.org/10.2514/1.G004710.
- [5] Lee, T., "Robust adaptive attitude tracking on SO(3) with an application to a quadrotor UAV," *IEEE Transactions on Control Systems Technology*, Vol. 21, No. 5, 2012, pp. 1924–1930. https://doi.org/10.48550/arXiv.1108.6031.
- [6] Simon, N., Ren, A. Z., Piqué, A., Snyder, D., Barretto, D., Hultmark, M., and Majumdar, A., "FlowDrone: wind estimation and gust rejection on UAVs using fast-response hot-wire flow sensors," *Proceedings of the 2023 IEEE International Conference on Robotics and Automation*, 2023, pp. 5393–5399. https://doi.org/10.48550/arXiv.2210.05857.
- [7] Hollenbeck, D., Nunez, G., Christensen, L. E., and Chen, Y., "Wind measurement and estimation with small unmanned aerial systems (sUAS) using on-board mini ultrasonic anemometers," *Proceedings of the 2018 International Conference of Unmanned Aircraft Systems*, 2018, pp. 285–292. https://doi.org/10.1109/ICUAS.2018.8453418.
- [8] Bailey, S. C. C., Sama, M. P., Canter, C. A., Pampolini, L. F., Lippay, Z. S., Schuyler, T. J., Hamilton, J. D., MacPhee, S. B., Rowe, I. S., Sanders, C. D., Smith, V. G., Vezzi, C. N., Wight, H. M., Hoagg, J. B., Guzman, M. I., and Smith, S. W., "University of Kentucky measurements of wind, temperature, pressure and humidity in support of LAPSE-RATE using multisite fixed-wing and rotorcraft unmanned aerial systems," *Earth System Science Data*, Vol. 12, No. 3, 2020, pp. 1759–1773. https://doi.org/10.5194/essd-12-1759-2020.
- [9] Brewer, M. J., and Clements, C. B., "Meteorological profiling in the fire environment using UAS," *Fire*, Vol. 3, No. 3, 2020, pp. 1–10. https://doi.org/10.3390/fire3030036.
- [10] Al-Ghussain, L., and Bailey, S. C., "An approach to minimize aircraft motion bias in multi-hole probe wind measurements made by small unmanned aerial systems," *Atmospheric Measurement Techniques*, Vol. 14, No. 1, 2021, pp. 173–184. https://doi.org/10.5194/amt-14-173-2021.
- [11] Yeo, D., Sydney, N., and Paley, D., "Onboard flow sensing for multi-rotor pitch control in wind," *Journal of Guidance, Control, and Dynamics*, Vol. 41, No. 5, 2018, pp. 1–6. https://doi.org/10.2514/1.G003102.
- [12] McConville, A., Richardson, T. S., and Moradi, P., "Comparison of multirotor wind estimation techniques through conventional on-board sensors," *Proceedings of the 2022 AIAA SciTech Forum and Exposition*, 2022, pp. 1–15. https://doi.org/10.2514/6.2022-0411.
- [13] Palomaki, R. T., Rose, N. T., van den Bossche, M., Sherman, T. J., and De Wekker, S. F., "Wind estimation in the lower atmosphere using multirotor aircraft," *Journal of Atmospheric and Oceanic Technology*, Vol. 34, No. 5, 2017, pp. 1183–1191. https://doi.org/10.1175/JTECH-D-16-0177.1.
- [14] Cassano, J. J., Seefeldt, M. W., Palo, S., Knuth, S. L., Bradley, A. C., Herrman, P. D., Kernebone, P. A., and Logan, N. J., "Observations of the atmosphere and surface state over Terra Nova Bay, Antarctica, using unmanned aerial systems," *Journal of Earth System Science Data*, Vol. 8, No. 1, 2016, pp. 115–126. https://doi.org/10.5194/essd-8-115-2016.
- [15] Allison, S., Bai, H., and Jayaraman, B., "Wind estimation using quadcopter motion: A machine learning approach," *Aerospace Science and Technology*, Vol. 98, No. 4, 2020, pp. 1–13. https://doi.org/10.1016/j.jweia.2022.105136.
- [16] Langelaan, J. W., Alley, N., and Neidhoefer, J., "Wind field estimation for small unmanned aerial vehicles," *Journal of Guidance, Control, and Dynamics*, Vol. 34, No. 4, 2011, pp. 1016–1030. https://doi.org/10.2514/1.52532.
- [17] González-Rocha, J., Woolsey, C. A., Sultan, C., and De Wekker, S. F. J., "Sensing wind from quadrotor motion," *Journal of Guidance, Control, and Dynamics*, Vol. 42, No. 4, 2019, pp. 836–852. https://doi.org/10.2514/1.G003542.
- [18] Shastry, A., and Paley, D. A., "UAV state and parameter estimation in wind using calibration trajectories optimized for observability," *IEEE Control System Letters*, Vol. 5, No. 5, 2021, pp. 1801–1806. https://doi.org/10.1109/LCSYS.2020.3044491.
- [19] Borup, K. T., Fossen, T. I., and Johansen, T. A., "A nonlinear model-based wind velocity observer for unmanned aerial vehicles," Proceedings of the 2016 International Federation of Automatic Control Symposium on Nonlinear Control Systems, Vol. 49, No. 18, 2016, pp. 276–283. https://doi.org/10.1016/j.ifacol.2016.10.177.

- [20] Waslander, S., and Wang, C., "Wind disturbance estimation and rejection for quadrotor position control," *Proceedings of the 2009 AIAA Infotech Aerospace Conference*, 2009, pp. 1–14. https://doi.org/10.2514/6.2009-1983.
- [21] Glasheen, K., Pinto, J., Steiner, M., and Frew, E., "Assessment of finescale local wind forecasts using small unmanned aircraft systems," *Journal of Aerospace Information Systems*, Vol. 17, No. 4, 2020, pp. 182–192. https://doi.org/10.2514/1.I010747.
- [22] Campbell, S. E., Clark, D. A., and Evans, J. E., "Preliminary weather information gap analysis for UAS operations," Tech. Rep. October, Lincoln Laboratory, Lexington, MA, 2017.
- [23] TruWeather Solutions, "TruWeather Solutions Prototypes Urban Weather Sensing Infrastructure," https://truweathersolutions.com/weather-sensing-infrastructure/, 2022. Accessed: 2023-10-05.
- [24] Gianfelice, M., Aboshosha, H., and Ghazal, T., "Real-time wind predictions for safe drone flights in Toronto," *Results in Engineering*, Vol. 15, No. September, 2022, pp. 1–15. https://doi.org/10.1016/j.rineng.2022.100534.
- [25] Vuppala, R. K., and Kara, K., "Wind field prediction in urban spaces for small unmanned aerial systems using convolutional autoencoders," *Proceedings of the 2022 AIAA AVIATION Forum*, 2022, pp. 1–13. https://doi.org/10.2514/6.2022-3605.
- [26] Galway, D., Etele, J., and Fusian, G., "Development and implementation of an urban wind field database for aircraft flight simulation," *Journal of Wind Engineering and Industrial Aerodynamics*, Vol. 103, No. April, 2012, pp. 73–85. https://doi.org/10.1016/j.jweia.2012.02.010.
- [27] Davoudi, B., Taheri, E., Duraisamy, K., Jayaraman, B., and Kolmanovsky, I., "Quad-rotor flight simulation in realistic atmospheric conditions," *AIAA Journal*, Vol. 58, No. 5, 2020, pp. 1992–2004. https://doi.org/10.2514/1.J058327.
- [28] Xue, M., and Wei, M., "Small UAV flight planning in urban environments," *Proceedings of the 2020 AIAA Aviation Forum*, 2021, pp. 1–12. https://doi.org/10.2514/6.2020-2890.
- [29] Cybyk, B. Z., McGrath, B. E., Frey, T. M., Drewry, D. G., Keane, J. F., and Patnaik, G., "Unsteady airflows and their impact on small unmanned air systems in urban environments," *Journal of Aerospace Information Systems*, Vol. 11, No. 4, 2014, pp. 178–194. https://doi.org/10.2514/1.I010000.
- [30] Galway, D., Etele, J., and Fusina, G., "Modeling of urban wind field effects on unmanned rotorcraft flight," *Journal of Aircraft*, Vol. 48, No. 5, 2011, pp. 1613–1620. https://doi.org/10.2514/1.C031325.
- [31] Ware, J., and Roy, N., "An analysis of wind field estimation and exploitation for quadrotor flight in the urban canopy layer," *Proceedings of the 2016 IEEE International Conference on Robotics and Automation*, 2016, pp. 1507–1514. https://doi.org/10.1109/ICRA.2016.7487287.
- [32] Patrikar, J., Dugar, V., Arcot, V., and Scherer, S., "Real-time motion planning of curvature continuous trajectories for urban UAV operations in wind," *Proceedings of the 2020 International Conference on Unmanned Aircraft Systems*, 2020, pp. 1254–1260. https://doi.org/10.1109/ICUAS48674.2020.9213837.
- [33] Orr, M. W., Rasmussen, S. J., Karni, E. D., and Blake, W. B., "Framework for developing and evaluating MAV control algorithms in a realistic urban setting," *Proceedings of the 2005 American Control Conference*, 2005, pp. 4096–4101. https://doi.org/10.1109/ACC.2005.1470619.
- [34] Raza, S. A., Sutherland, M., Etele, M., and Fusina, G., "Experimental validation of quadrotor simulation tool for flight within building wakes," *Aerospace Science and Technology*, Vol. 67, No. August, 2017, pp. 169–180. https://doi.org/10.1016/j.ast. 2017.03.043.
- [35] Baskar, D., and Gorodetsky, A., "A simulated wind-field dataset for testing energy efficient path-planning algorithms for UAVs in urban environment [Data set]," *University of Michigan Deep Blue Data*, 2020, pp. 1–2. https://doi.org/10.7302/pdcv-0x63.
- [36] Langelaan, J. W., Spletzer, J., Montella, C., and Grenestedt, J., "Wind field estimation for autonomous dynamic soaring," Proceedigns of the 2012 IEEE International Conference on Robotics and Automation, 2012, pp. 16–22. https://doi.org/10.1109/ ICRA.2012.6224954.
- [37] Rodriguez, L., Cobano, J. A., and Ollero, A., "Wind field estimation and identification having shear wind and discrete gusts features with a small UAS," *Proceedings of the 2016 IEEE/RSJ International Conference on Intelligent Robots and Systems*, 2016, pp. 5638–5644. https://doi.org/10.1109/IROS.2016.7759829.
- [38] Luders, B., Sugel, I., and How, J. P., "Robust trajectory planning for autonomous parafoils under wind uncertainty," *Proceedings of the 2013 AIAA Infotech* @ *Aerospace Conference*, 2013, pp. 1–27. https://doi.org/10.2514/6.2013-4584.

- [39] Tian, P., Chao, H., Rhudy, M., Gross, J., and Wu, H., "Wind sensing and estimation using small fixed-wing unmanned aerial vehicles: A survey," *Journal of Aerospace Information Systems*, Vol. 18, No. 3, 2021, pp. 132–143. https://doi.org/10.2514/1. I010885.
- [40] Sydney, N., Smyth, B., and Paley, D. A., "Dynamic control of autonomous Quadrotor flight in an estimated wind field," Proceedings of the 2013 IEEE Conference on Decision and Control, 2013, pp. 3609–3616. https://doi.org/10.1109/CDC.2013. 6760438
- [41] Department of Defense, "Flying Qualities of Piloted Aircraft," MIL-STD-1797A, Vol. Notice 3, 2004, pp. 678–702.
- [42] Beal, T., "Digital simulation of atmospheric turbulence for Dryden and von Karman models," *Journal of Guidance, Control, and Dynamics*, Vol. 16, No. 1, 1993, pp. 132–138. https://doi.org/10.2514/3.11437.
- [43] Hess, R. A., "Rotorcraft handling qualities in turbulence," *Journal of Guidance, Control, and Dynamics*, Vol. 18, No. 1, 1995. https://doi.org/10.2514/3.56654.
- [44] Anderson, R. P., Bakolas, E., Milutinović, D., and Tsiotras, P., "Optimal feedback guidance of a small aerial vehicle in a stochastic wind," *Journal of Guidance, Control, and Dynamics*, Vol. 36, No. 4, 2013, pp. 975–985. https://doi.org/10.2514/1.59512.
- [45] Dalmau, R., Prats, X., and Baxley, B., "Using broadcast wind observations to update the optimal descent trajectory in real-time," *Journal of Air Transportation*, Vol. 28, No. 3, 2020, pp. 82–92. https://doi.org/10.2514/1.D0174.
- [46] Peterson, C. K., and Paley, D. A., "Distributed estimation for motion coordination in an unknown spatiotemporal flowfield," *Proceedings of the 2011 AIAA Guidance, Navigation, and Control Conference*, 2011, pp. 1–11. https://doi.org/10.2514/1.59453.
- [47] Lan, X., and Schwager, M., "Rapidly exploring random cycles: persistent estimation of spatiotemporal fields with multiple sensing robots," *IEEE Transactions on Robotics*, Vol. 32, No. 5, 2016, pp. 1230–1244. https://doi.org/10.1109/TRO.2016.2596772.
- [48] Lee, K. M. B., Yoo, C., Hollings, B., Anstee, S., Huang, S., and Fitch, R., "Online estimation of ocean current from sparse GPS data for underwater vehicles," *Proceedings of the 2019 International Conference on Robotics and Automation*, 2019, pp. 3443–3449. https://doi.org/10.1109/ICRA.2019.8794308.
- [49] Yang, S., Wei, N., Jeon, S., Bencatel, R., and Girard, A., "Real-time optimal path planning and wind estimation using Gaussian process regression for precision airdrop," *Proceedings of the 2017 American Control Conference*, 2017, pp. 2582–2587. https://doi.org/10.23919/ACC.2017.7963341.
- [50] Hollinger, G. A., Pereira, A. A., Binney, J., Somers, T., and Sukhatme, G. S., "Learning uncertainty in ocean current predictions for safe and reliable navigation of underwater vehicles," *Jorunal of Field Robotics*, Vol. 33, No. 1, 2014, pp. 47–66. https://doi.org/10.1002/rob.21613.
- [51] Lawrance, N. R., and Sukkarieh, S., "Path planning for autonomous soaring flight in dynamic wind fields," *Proceedings of the 2011 IEEE International Conference on Robotics and Automation*, 2011, pp. 2499–2505. https://doi.org/10.1109/ICRA.2011.5979966.
- [52] Patterson, M. A., and Rao, A. V., "GPOPS-II: A MATLAB software for solving multiple-phase optimal control problems Using hp-adaptive Gaussian quadrature collocation methods and sparse nonlinear programming," *Association for Computing Machinery: Transactions on Mathematical Software*, Vol. 41, No. 1, 2014, pp. 1–37. https://doi.org/10.1145/2558904.
- [53] R. Beard, T. M., Small Unmanned Aircraft: Theory and Practice, Princeton University Press, Princeton, 2012.
- [54] Olea, R. A., Geostatistics for Engineers and Earth Scientists, Springer US, New York, 1999.
- [55] Jadaliha, M., Xu, Y., Choi, J., Johnson, N. S., and Li, W., "Gaussian process regression for sensor networks under localization uncertainty," *IEEE Transactions on Signal Processing*, Vol. 61, No. 2, 2012, pp. 223–237. https://doi.org/10.1109/TSP.2012. 2223695.
- [56] Rasmussen, C., and Williams, C., Gaussian Processes for Machine Learning, MIT Press, Boston, 2006.
- [57] Xu, Y., Choi, J., and Oh, S., "Mobile sensor network navigation using Gaussian processes with truncated observations," *IEEE Transactions on Robotics*, Vol. 27, No. 6, 2011, pp. 1118–1131. https://doi.org/10.1109/TRO.2011.2162766.
- [58] Patterson, M. A., and Rao, A. V., "GPOPS-II: A general-purpose MATLAB software for solving multiple-phase optimal control problems," https://gpops2.com/resources/gpops2UsersGuide.pdf, 2016. Accessed: 2023-10-29.
- [59] MathWords, "ode45: Solve nonstiff differential equations medium order method," https://www.mathworks.com/help/matlab/ref/ode45.html, 2023. Accessed: 2023-11-22.